















Three-dimensional diffractive acoustic tomography

Received: 7 June 2024

Accepted: 20 January 2025

Published online: 29 January 2025

 Check for updates


Luca Menozzi ^{1,12}, Tri Vu^{1,12}, Aidan J. Canning^{1,12}, Harshal Rawtani ², Carlos Taboada^{1,3}, Marie Elise Abi Antoun⁴, Chenshuo Ma¹, Jesse Delia⁵, Van Tu Nguyen ¹, Soon-Woo Cho ¹, Jianing Chen ¹, Theresa Charity ^{6,7}, Yirui Xu¹, Phuong Tran^{1,8}, Jun Xia ⁹, Gregory M. Palmer ^{6,7}, Tuan Vo-Dinh ^{1,10} , Liping Feng ²  & Junjie Yao ^{1,11} 

Acoustically probing biological tissues with light or sound, photoacoustic and ultrasound imaging can provide anatomical, functional, and/or molecular information at depths far beyond the optical diffusion limit. However, most photoacoustic and ultrasound imaging systems rely on linear-array transducers with elevational focusing and are limited to two-dimensional imaging with anisotropic resolutions. Here, we present three-dimensional diffractive acoustic tomography (3D-DAT), which uses an off-the-shelf linear-array transducer with single-slit acoustic diffraction. Without jeopardizing its accessibility by general users, 3D-DAT has achieved simultaneous 3D photoacoustic and ultrasound imaging with optimal imaging performance in deep tissues, providing near-isotropic resolutions, high imaging speed, and a large field-of-view, as well as enhanced quantitative accuracy and detection sensitivity. Moreover, powered by the fast focal line volumetric reconstruction, 3D-DAT has achieved 50-fold faster reconstruction times than traditional photoacoustic imaging reconstruction. Using 3D-DAT on small animal models, we mapped the distribution of the biliverdin-binding serpin complex in glassfrogs, tracked gold nanoparticle accumulation in a mouse tumor model, imaged genetically-encoded photoswitchable tumors, and investigated polyfluoroalkyl substances exposure on developing embryos. With its enhanced imaging performance and high accessibility, 3D-DAT may find broad applications in fundamental life sciences and biomedical research.

Photoacoustic (PA) and ultrasound (US) imaging, using light and sound, respectively, are non-invasive non-ionizing modalities that provide complementary information in deep tissues. PA imaging can map the optical absorption contrast by exciting the tissue with short

laser pulses^{1–3}. The diffused optical energy absorbed by tissue molecules (e.g., hemoglobin, melanin, fat) is partially or completely converted into heat, resulting in ultrasound waves via thermoelastic expansion. The ultrasound waves can then be detected by an

¹Department of Biomedical Engineering, Duke University, Durham, NC, USA. ²Duke University School of Medicine, Durham, NC, USA. ³Department of Biological Sciences, Vanderbilt University, Nashville, TN, USA. ⁴Tufts Medical Center, Boston, Massachusetts, USA. ⁵American Museum of Natural History, New York City, New York, USA. ⁶Department of Radiation Oncology, Duke University School of Medicine, Durham, NC 27710, USA. ⁷Department of Surgery, Duke University School of Medicine, Durham, NC 27710, USA. ⁸Department of Biomedical Engineering, North Carolina State University, Raleigh, NC, USA. ⁹Department of Biomedical Engineering, University at Buffalo, Buffalo, New York, USA. ¹⁰Department of Chemistry, Duke University, Durham, NC 27708, USA. ¹¹Department of Neurology, Duke University School of Medicine, Durham, NC 27710, USA. ¹²These authors contributed equally: Luca Menozzi, Tri Vu, Aidan J. Canning.

 e-mail: tuan.vodinh@duke.edu; liping.feng@duke.edu; junjie.yao@duke.edu

ultrasound transducer array and reconstructed into a tomographic image that maps the original light deposition inside the tissues⁴. By tuning the excitation wavelength, photoacoustic imaging can spectroscopically unmix different tissue components⁵. US imaging, on the other hand, can visualize the anatomical structure of deep tissues by transmitting short-pulsed ultrasound waves and detecting the boundaries of differing acoustic impedances. Using the same ultrasound transducer, PA and US imaging can be readily integrated into a single device with inherent image co-registration, allowing for functional, molecular, and structural imaging in deep tissues for various life science applications^{6,7}.

Ultrasound detection is one of the major factors in PA/US imaging that determines the spatial resolution, field-of-view (FOV), imaging speed, cost, and accessibility of the system. For example, ring-array transducers with panoramic ultrasound detection can provide high-quality 2D images^{8,9}, but are difficult to adapt for high-throughput experimental settings¹⁰. Hemispherical-array transducers can produce high-quality 3D images¹¹, but often have a small densely sampled FOV¹². Although ring- and hemispherical-array-based imaging systems have found important clinical applications, such as breast cancer imaging¹³, their broad clinical translation is likely impeded by their relatively complex operation, high cost, and limited access to different anatomical locations, especially for handheld applications^{14,15}.

In contrast, linear-array transducers are most commonly used for PA/US imaging^{15,16}. These linear-array transducers are off-the-shelf, cost-effective, simple to set up, easy to operate, and allow for imaging of almost any geometries (skin, neck, breast, brain, etc.). Therefore, it is generally agreed that PA/US systems with linear-array transducers have the best clinical translation potential¹⁷. However, 3D PA/US imaging systems that are linear-array-based have worse image quality when compared with ring- or hemispherical-array-based systems¹⁸, mostly due to the fixed acoustic lens with poor elevational resolution and detection sensitivity. Recently, deep-learning-based methods have been proposed to improve linear-array-based PA imaging¹⁹. However, the lack of high-quality training data makes these approaches vulnerable to the ‘hallucination effect’, particularly for in vivo applications where the ground truth is not always available for high-fidelity training^{20–22}.

Single-slit diffraction was previously applied to improve linear-array-based photoacoustic imaging^{23–25}. However, this concept has not yet been applied to ultrasound imaging, or functional and molecular photoacoustic imaging. Moreover, the impact of the slit geometry on the spatial resolution, signal-to-noise ratio (SNR) and contrast has not been characterized. The previous work also had a high computational burden and long reconstruction time. Here, we develop, characterize, and validate a slit-based technique for diffraction-enhanced PA and US imaging using an off-the-shelf linear-array transducer—3D diffractive acoustic tomography (3D-DAT). 3D-DAT provides near-isotropic spatial resolutions for both 3D US and PA imaging by creating a synthetic matrix aperture via single-slit diffraction. The synthetic matrix aperture has more than 50,000 elements, which is ~50-fold of a typical piezo matrix array in PA/US imaging (e.g., 1064 elements)²⁶, without sacrificing the detection sensitivity or increasing the system cost.

Furthermore, we develop a graphics processing unit (GPU) - powered fast focal line (FFL) image reconstruction method, which accelerates the 3D image reconstruction by over 50-fold compared with previously reported methods²⁷, allowing for high-throughput applications. FFL is an efficient implementation of the focal line reconstruction²⁸, where the reconstruction is formulated as GPU-accelerated sparse matrix multiplication²⁹. In FFL, the synthetic aperture acquisitions are parallelized along the columns of the sparse matrix. Additionally, by investigating the effect of synthetic aperture size on the final image quality, the efficiency of FFL is further increased two-fold while maintaining the image quality.

3D-DAT has two working modes: diffractive photoacoustic tomography (DPAT) and diffractive ultrasound tomography (DUST).

3D-DAT can flexibly control the acoustic diffraction pattern, allowing for adjusting the slit width to balance between the gain in spatial resolution and the loss in acoustic energy. Through comprehensive numerical simulations, phantom studies, and in vivo experiments, we demonstrate 3D-DAT’s enhanced imaging performance over traditional PA/US imaging. Enabled by 3D-DAT, we mapped the whole-body distribution of the biliverdin-binding serpin complex in glassfrogs, which plays a major role in the frog’s coloration³⁰. We also monitored the circulation and intratumoral accumulation of caged gold nanostars (cGNS) in a mouse tumor model, with nano-molar-level detection sensitivity. Furthermore, we performed differential imaging of genetically encoded photoswitching tumors in vivo. Lastly, we applied 3D-DAT to study the embryonic microenvironment during normal pregnancy and investigated the adverse effect of per- and poly-fluoroalkyl substances (PFAS) exposure on embryo development. All these biomedical applications have collectively demonstrated the improved imaging capability offered by 3D-DAT, which is expected to provide a powerful and accessible research platform for studying life sciences.

Results

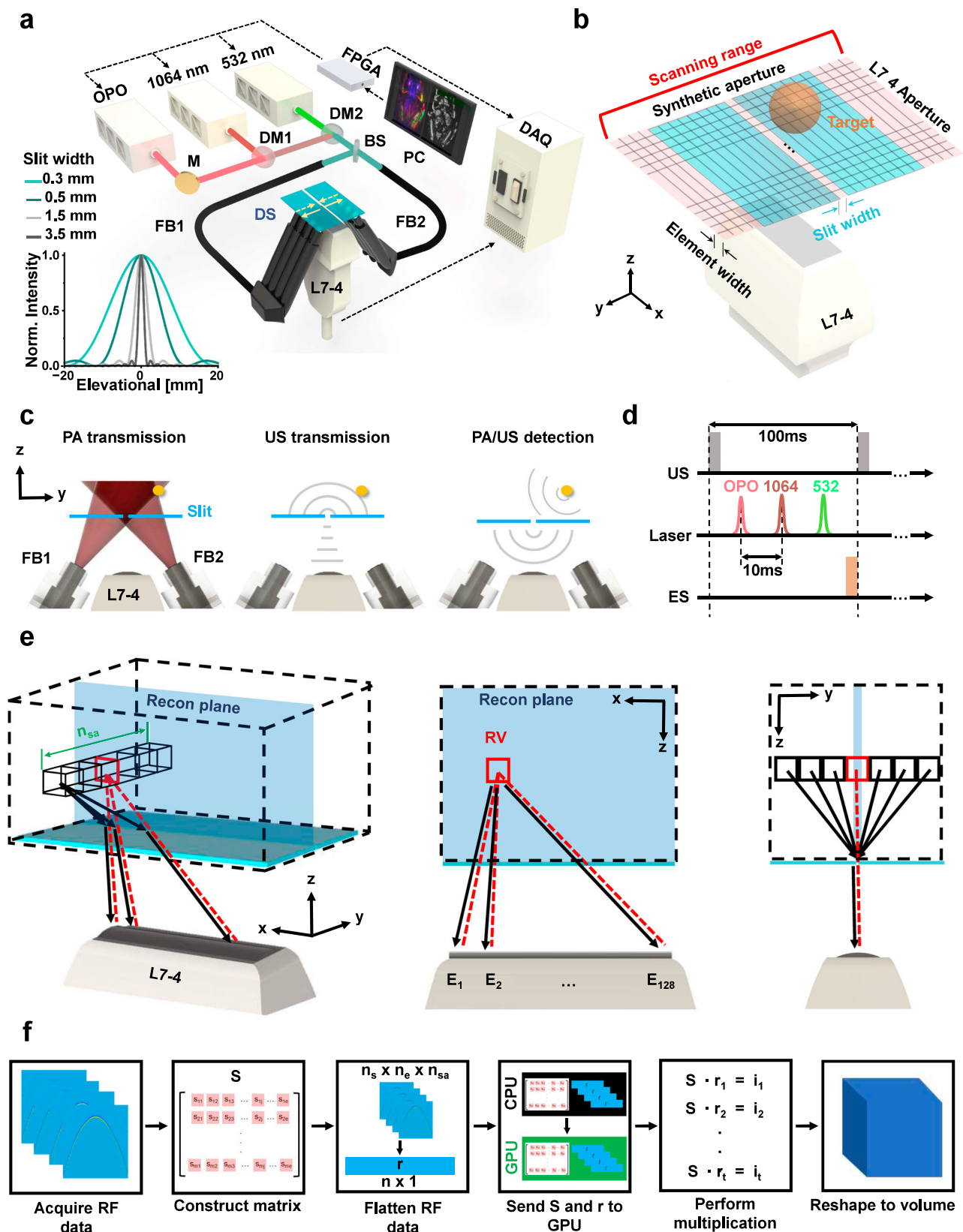
Principle of 3D-DAT

3D-DAT has three major system modules (Fig. 1a): multi-wavelength optical illumination, ultrasound transmission, and detection, and the dynamic diffractive slit. Combining these three modules allows for functional and molecular PA imaging and structural US imaging with near-isotropic resolutions (Supplementary Fig. 1) and detection sensitivity. In 3D-DAT, a representative off-the-shelf linear-array transducer (L7-4, Philips) was adapted to balance the spatial resolution and imaging depth. A transparent glass slit is positioned at the elevational focus of the linear-array transducer to provide diffractive ultrasound transmission and reception (refer to Methods for more details on the slit). By scanning the linear-array transducer and the slit together along the elevational axis across the sample, a synthetic matrix aperture can be generated, and the complete dataset is used for 3D image reconstruction (Fig. 1b). With the slit controlled by a high-precision motorized stage, we can precisely adjust the slit width (Supplementary Movie 1). The slit width determines the elevational element size and the elevational diffraction angle. The linear-array transducer’s lateral aperture determines the total synthetic aperture length, and the elevational scanning range determines the total synthetic aperture width.

3D-DAT has two working modes: DPAT for 3D PA imaging and DUST for 3D US imaging. In DPAT mode, we use three separate lasers to provide wide-field optical illumination (~8 cm² at the target surface) with a broad optical wavelength range (532 nm, 668–1000 nm, and 1064 nm) (Fig. 1c). In DUST mode, a plane acoustic wave is transmitted by the linear-array transducer, which is then diffracted by the slit into an approximately cylindrical wave to probe a large sample volume. In both DPAT and DUST modes, the slit redirects the returning wave toward the linear-array transducer from its elevational focus, allowing for detecting the signals originating within a large elevational angle. The broadened elevational detection aperture improves the elevational spatial resolution (Supplementary Note 1, Supplementary Movie 2 and Supplementary Figs. 2, 3). By precisely synchronizing the laser firing and the ultrasound transmission, DPAT and DUST can be performed concurrently at each elevational scanning position (Fig. 1d, Supplementary Fig. 4).

Principle of fast focal line (FFL) reconstruction

We have developed an FFL reconstruction method based on the focal line geometry, providing 3D PA and US imaging with near-isotropic resolutions^{28,31} (Fig. 1e). Briefly, PA and US signals acquired at consecutive elevational scanning positions are used for beamforming based on the 3D delay-and-sum method. Unlike traditional PA/US imaging, the wave propagation path in FFL is calculated by connecting



the reconstruction voxel to the slit opening, and then from the slit opening to the transducer. The large number of synthetic aperture elements and reconstruction voxels results in time-consuming reconstructions. To increase computational speed, our algorithm applies a sparse matrix multiplication operation for each reconstructed frame, as $\mathbf{S} \cdot \mathbf{r} = \mathbf{f}$. Here, \mathbf{S} is a highly sparse matrix (>99% sparsity) of size

$m \times n$, where m is the number of voxels in the reconstruction volume and n is the total number of signal samples from all transducer elements of the synthetic aperture. \mathbf{S} is effectively a beamforming matrix that performs a 3D delay-and-sum operation via a single matrix multiplication. Vector \mathbf{r} is the signal data of size $n \times 1$. Vector \mathbf{f} is the resultant vectorized image, which can be reshaped into the 3D

Fig. 1 | Principle of 3D-DAT and FFL reconstruction. **a** Schematic of 3D-DAT system with a linear-array transducer and dynamic slit control. Note that the slit is positioned at the elevational focus of the linear-array transducer. The inset shows the far-field acoustic diffraction pattern with varying slit widths, simulated by Fraunhofer approximations. BS, beam splitter; DM, dichroic mirror; DS, dynamic slit; FB, fiber bundle; OPO, optical parametric oscillator (668–1000 nm). **b** Principle of 3D-DAT generating a synthetic matrix aperture by scanning the linear-array transducer with the slit along the elevational axis of the transducer. Each scanning position provides one row of synthetic matrix elements. **c** 3D-DAT in DPAT and DUST mode. For DPAT mode, the light illumination directly transmits through the slit plate (which is made of glass) onto the target surface. For DUST mode, the

transmitted acoustic waves pass through the slit opening and form a diffraction pattern before arriving at the target surface. In both modes, broad-angle detection of the acoustic waves from the target is achieved by single-slit diffraction.

d Triggering sequence of the 3D-DAT system, including DUST and multi-wavelength DPAT. ES, elevational scanning. **e** Geometry of FFL reconstruction. Beamforming is performed along both elevational and lateral axes, which allows for an increased detection aperture width and thus improved resolution. n_{sa} , number of synthetic aperture elements. RV, reconstructed voxel. E, element. **f** Pipeline of GPU-accelerated FFL reconstruction. The sparse matrix S is calculated only once and used for reconstruction by matrix multiplication with the vectorized RF data.

reconstructed image (Supplementary Fig. 5). The matrix multiplication is repeated for each scanning position to generate the complete 3D reconstruction (Fig. 1f). The reconstruction speed of FFL is further improved by using GPUs when performing matrix multiplications. Additionally, by identifying the minimum synthetic aperture width needed for efficient image reconstruction, FFL has achieved a 50-fold improvement in computation speed compared to traditional methods (Supplementary Note 2 and Supplementary Fig. 6). The FFL algorithm is applied to both DPAT and DUST. For DPAT, one-way wave propagation is calculated for each reconstructed voxel. For DUST, round-trip propagation is used in the path length calculation. Note that sparse matrix multiplication may be applied to other ultrasound or photo-acoustic reconstructions to improve reconstruction speed, independent of the dimensionality or the detector geometry.

Characterization of 3D-DAT

The advantage of 3D-DAT over traditional PA/US imaging stems from the slit-enabled acoustic diffraction. The Fraunhofer approximation gives the far-field diffraction pattern in 3D-DAT as the Fourier transform of the slit opening³², showing the main-lobe width of the diffraction pattern is inversely proportional to the slit width. A smaller slit width produces a larger acoustic wave angle along the elevational axis, resulting in an increased detection angle along this axis. The broader detection angle is beneficial for beamforming, as it allows for a larger total effective aperture to be used in the reconstruction (Supplementary Note 1 and Supplementary Figs. 2 and 7), leading to improved elevational resolution.

Inserting a slit in the acoustic path results in the partial rejection of acoustic energy that would otherwise be received by the transducer. Thus, we investigated the impact of the slit on the received acoustic pressure through simulations. We also compared traditional imaging with 3D-DAT with different slit widths (Supplementary Fig. 8). We found that, with a slit width of 0.8 mm, the received acoustic pressure from an in-plane point target in 3D-DAT decreased by ~75% when compared to that in traditional imaging. However, the off-axis acceptance angle of this point target increased by almost ten times when scanning across the elevational aperture (Fig. 2a, b and Supplementary Fig. 8). Collectively, these two competing factors provided 3D-DAT with a comparable total acoustic pressure received across the elevational scanning aperture.

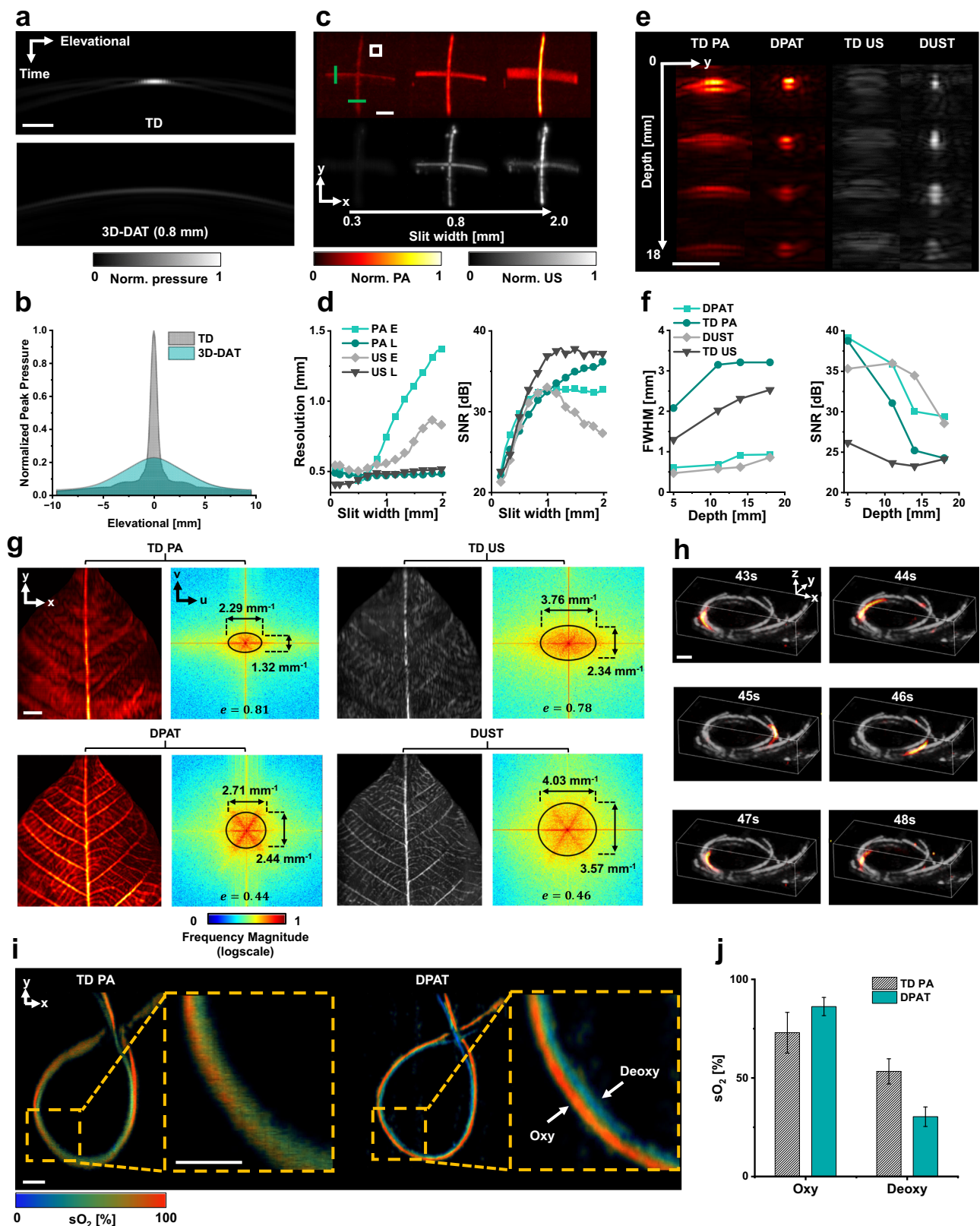
To investigate the relationship between slit width and imaging performance of 3D-DAT, we first performed simulations of a crosshair target with different slit widths (Supplementary Fig. 9). We then experimentally imaged a similar crosshair target with the slit width ranging from 0.08 mm to 2.0 mm (Fig. 2c, Supplementary Note 3, Supplementary Movie 3, and Supplementary Movie 4). The simulation and experimental results agreed well. The spatial resolution and SNR as a function of slit width were quantified for both the lateral and elevational axes (Fig. 2d). Additionally, the CNR as a function of the slit width was quantified, showing a similar trend with the SNR (Supplementary Fig. 10 and Supplementary Note 4).

As we gradually increase the slit width from 0.08 mm to 2.0 mm and keep the elevational scanning range of 20 mm, 3D-DAT can be

broadly characterized into three regimes: the scanning-range-dominated regime, the slit-width-dominated regime, and the acoustic-lens-dominated regime (Supplementary Fig. 11). In the scanning-range-dominated regime, the slit width (0–0.5 mm) is so small that the diffraction pattern's main lobe is larger than the scanning range (20 mm). Here, 3D-DAT achieves the best elevational resolution of ~400 μm , which is mainly limited by the scanning range. However, the SNR is relatively low regardless of the target orientation, due to acoustic energy blocked by the narrow slit. In the slit-width-dominated regime, the slit width (0.5–1.8 mm) is large enough so that the diffraction pattern's main lobe is smaller than the scanning range but still larger than the transducer's elevational focusing. The elevational resolution is approximately proportional to the slit width (Supplementary Note 1). The SNR plateaus in DPAT mode and peaks in DUST mode, due to a combined result of increased acoustic energy through the slit and a relatively large receiving angle. In the acoustic-lens-dominated regime, the slit width (>1.8 mm) is larger than the elevational focus of the transducer, resulting in negligible diffraction effect. The elevational resolution is determined by the elevational focusing, as in the traditional PA/US imaging. As expected, the lateral resolution of 3D-DAT has no dependence on the slit width (Fig. 2d and Supplementary Fig. 9).

To balance the improvement in elevational resolution and the potential loss in SNR, we have chosen 0.8 mm as the optimal slit width for all following studies in this work. We further demonstrated that 3D-DAT's performance is consistent at different depths by imaging graphite targets (Fig. 2e and Supplementary Fig. 12). The elevational FWHM of the graphite with DPAT is consistent at <1 mm at all measured depths, while the FWHM of the graphite with traditional PA imaging deteriorated from ~2 mm at 0 mm depth to ~3 mm at 2 cm depth (Fig. 2f). Similarly, the elevational FWHM of the graphite with DUST remained at <1 mm at all depths, while the elevational FWHM of the graphite with traditional US imaging ranged from ~1 mm at superficial depths to ~2 mm at deeper depths. The SNR of both DPAT and DUST modes is greater than or equal to the SNR in the traditional PA/US imaging at depths up to 2 cm, with the CNR showing similar trends (Supplementary Fig. 10).

Isotropic spatial resolutions are crucial in 3D imaging to faithfully reflect the tissue's true anatomy. We imaged a star phantom using DPAT (Supplementary Fig. 13), clearly showing the difference provided by the anisotropic resolution of traditional PA imaging and the near-isotropic resolution of DPAT. The performance of 3D-DAT on more complex targets was validated by imaging a leaf-skeleton phantom (Fig. 2g). The fine, branching structures are mostly unresolvable in traditional PA and US imaging, while 3D-DAT can better recover these fine structures. We analyzed the spatial frequency spectrum of the skeleton leaf images along the lateral and elevational axes for both the PA and US imaging mode. We observed more isotropic distribution of spatial frequencies in 3D-DAT images compared to traditional PA and US images. By fitting an ellipse to the spatial frequency distribution, we observed a ~46% and ~41% reduction in elliptical eccentricity by 3D-DAT in the DPAT and DUST mode, respectively (Fig. 2g), indicating that a relatively uniform distribution of the spatial frequency contents is achieved by 3D-DAT. We also implemented 3D-DAT using another



widely available linear-array transducer (9L-D, GE Healthcare) (Supplementary Fig. 14), indicating that 3D-DAT can be potentially applied with a large arsenal of off-the-shelf linear-array transducers.

High volumetric imaging speed with a large FOV is critically important for capturing the tissue's dynamic responses to various physiological or pathological challenges. We demonstrated high-

speed 3D-DAT with a 3D frame rate of 1 Hz over an FOV of $40 \times 14 \times 15 \text{ mm}^3$ (Fig. 2h). A bolus of blood was flowing through a spiral-patterned silicon tube that was embedded in an optically scattering medium (Supplementary Movie 5). The slit and transducer were scanned with a step size of 0.14 mm. We used a 1064 nm laser for DPAT with a high pulse repetition rate of 100 Hz. The entire FOV was imaged

Fig. 2 | Characterization of 3D-DAT. **a** Simulated acoustic signal from a point source detected by traditional PA imaging with a linear-array transducer or 3D-DAT. Envelope detection is applied to the simulated acoustic signal. **b** Peak pressure from the point source detected across the elevational aperture. While traditional imaging shows 4-fold stronger on-axis peak pressure, 3D-DAT achieves 10-fold wider receiving angle. **c** Experimental DPAT (top) and DUST (bottom) images of a crosshair phantom, with three representative slits widths. Note the elevational (y-axis) resolution deteriorates with the increasing slit width for both DPAT and DUST. **d** Experimental spatial resolution and SNR of DPAT and DUST, as a function of the slit width. E, elevational; L, lateral. **e** Traditional PA/US imaging and 3D-DAT (slit width: 0.8 mm) of a graphite phantom at different depths. TD PA, traditional PA imaging; TD US, traditional US imaging. **f** Depth-dependent FWHM and SNR of the

graphite phantom with traditional PA/US imaging and 3D-DAT. **g** Traditional and 3D-DAT images of a leaf skeleton phantom (left) with the corresponding spatial frequency spectra (right). The 3D-PAT images have near-isotropic resolution and near-symmetric frequency distribution. **h** Snapshot images of high-speed 3D-DAT of a bolus blood flowing through a spiral tube embedded in optically scattering medium. Both DUST (shown in gray) and DPAT (shown in color) images were acquired at 1 Hz, with an FOV of $40 \times 14 \times 15 \text{ mm}^3$. **i** Oxygenation images of blood-filled tubes by DPAT and traditional PA imaging. HbO₂, oxy-hemoglobin; HbR, deoxy-hemoglobin. **j** Quantification of the average oxygen saturation of the blood tubes by traditional PA imaging and DPAT ($n = 1038$ pixels for each tube). Error bars show standard deviation. Scale bars, 2 mm for (a)–(e), 5 mm for (g)–(i).

at 1 Hz, showing the flowing blood through the spiral tube, with an estimated flow speed of ~6 mm/s (Supplementary Movie 6).

We then evaluated the functional imaging capability of DPAT on a pair of closely positioned blood-filled tubes with different oxygenation levels (Fig. 2i). We found that for both tubes, DPAT was able to accurately estimate the blood oxygenation while traditional PA imaging failed (Fig. 2j and Supplementary Note 5). With traditional PA imaging, the measured oxygen saturation of hemoglobin (sO₂) was inaccurate with an average measurement error of ~28% (Supplementary Fig. 15). Tube segments that were not aligned with the elevational axis were greatly blurred in traditional PA imaging, which introduced significant error in quantitative analysis. By contrast, DPAT was able to clearly distinguish oxygenated and deoxygenated blood consistently along the tubes, with an average error of ~14%. The improvement in sO₂ quantification by DPAT is important for in vivo functional and molecular imaging.

Validation of 3D-DAT for in vivo Imaging

We demonstrated the enhanced anatomical, functional, and molecular imaging of 3D-DAT using several proof-of-concept experiments in small animals (Supplementary Note 6). Firstly, photoacoustic imaging is well-suited for biological research of small amphibians with naturally rich colors. We previously applied photoacoustic imaging to reveal the mechanism that allows glassfrogs to maintain transparency during sleep³³. Here, we further demonstrate that 3D-DAT can be a useful tool to study glassfrogs of the species *Hyalinobatrachium fleischmanni* in vivo (Supplementary Movie 7). We can observe significantly improved structural clarity, as a result of enhanced elevational resolution, with 3D-DAT compared to traditional PA and US imaging (Supplementary Fig. 16). This enhancement in image clarity is again shown in the spatial frequency spectrum of the images, where a relatively uniform and direction-independent distribution in the frequency contents can be observed by 3D-DAT (Supplementary Fig. 17). In the traditional PA image, blood vessels were blurred or even missing along the elevational axis (Fig. 3a). By contrast, DPAT imaged more vessels, regardless of the vessel orientations. Multi-wavelength DPAT revealed different endogenous contrasts of the glassfrog essential for the frog's coloration, including the hemoglobin in the blood vessels, melanin in the eyes, and the cyan-colored biliverdin-binding serpins (BBS) in the bones, skin, and lymph. Using a representative blood vessel aligned with the lateral axis, the DPAT image shows a ~59% decrease in the elevational FWHM compared to the traditional PA image (Fig. 3b). We also quantified the SNR of three representative regions of interest in the glassfrog: an elevationally aligned blood vessel (R1), a laterally aligned blood vessel (R2), and a BBS-rich area in the dorsal skin (R3). Compared to the traditional PA image, the DPAT image has higher SNR in R1, R2, and R3 by 1.82 dB, 7.57 dB, and 1.96 dB, respectively (Fig. 3c). Similarly, the DUST image shows improved image quality of the internal organs of the glassfrog, such as the lungs and bones (Fig. 3d). The boundaries of the lungs can be clearly delineated with relatively uniform echogenicity. Using a representative bone aligned with the

lateral axis, the DUST image shows a ~49% decrease in its elevational FWHM compared to the traditional US image (Fig. 3e). The SNR was also quantified using three representative structures in the frog: an elevationally aligned bone (R1), a laterally aligned bone (R2), and a region of the lung surface (R3). Traditional US and DUST images show similar SNRs in all regions (Fig. 3f).

We further tested 3D-DAT for whole-body mouse imaging (Fig. 3g, h and Supplementary Figs. 18 and 19). As expected, DPAT can resolve both superficial and deep blood vessels (up to 10 mm depth), regardless of the vessel orientation, while traditional PA imaging suffered from the poor visibility of the elevational vessels (Fig. 3g), with a ~62% decrease in the FWHM of the elevational vessels (Supplementary Fig. 19b). DPAT can achieve similar imaging depths in mice with traditional PA imaging, which was consistent with our phantom studies. Additionally, the DPAT image shows a slight reduction in SNR by ~1.1 dB, evaluated over three representative regions (Supplementary Fig. 20). DUST also shows a clear improvement in spatial resolution over the traditional US imaging, evident by resolving the individual vertebrae in the spinal cord (Fig. 3h and Supplementary Fig. 18). This was quantified as a ~40% reduction in FWHM in the vertebrae (Supplementary Fig. 19d). DUST likewise shows comparable imaging depth with traditional US in mice. The DUST image shows an increase in SNR by ~4.6 dB, evaluated over three representative regions (Supplementary Fig. 20). Additionally, we calculated CNR using the same in vivo regions used to evaluate SNR for both the frog and mouse images and found similar trends in CNR with SNR (Supplementary Fig. 20), consistent with our phantom studies (Supplementary Fig. 10).

To demonstrate 3D-DAT's functional imaging capability with a high volumetric speed, we imaged a mouse undergoing hypoxia challenges (Supplementary Fig. 21). A region of $40 \times 14 \times 15 \text{ mm}^3$ over the liver region was scanned at a volumetric rate of 1 Hz. For this study, only the 1064 nm laser was used, taking advantage of its high pulse repetition frequency of 100 Hz. Since oxy-hemoglobin's absorption at 1064 nm is 10-fold stronger than deoxy-hemoglobin, DPAT signal intensity at 1064 nm can be used to approximate the change in the oxygenated blood volume. DPAT at 1064 nm was performed over three cycles of normoxia (21% O₂, 79% N₂; 3.5 min) and hypoxia (2% O₂, 98% N₂; 30 s)³⁴ (Supplementary Fig. 21a). The liver region shows a substantial reduction in the oxygenated blood volume under hypoxia, with an average signal decrease by ~50% (Supplementary Fig. 21b, c). This result shows the feasibility of fast functional imaging by 3D-DAT with a large FOV for imaging dynamic biological processes in vivo.

Functional and molecular 3D-DAT of a mouse tumor model

An important advantage of photoacoustic imaging is the inherent molecular sensitivity. By tuning the excitation wavelengths, PA imaging allows for mapping the biodistribution of exogenous molecules^{35–39}. Gold nanostars (GNS) are of interest as a PA molecular contrast for tumor imaging, due to their efficient photothermal effect in the near-infrared wavelength region^{40,41}. Caged gold nanostars

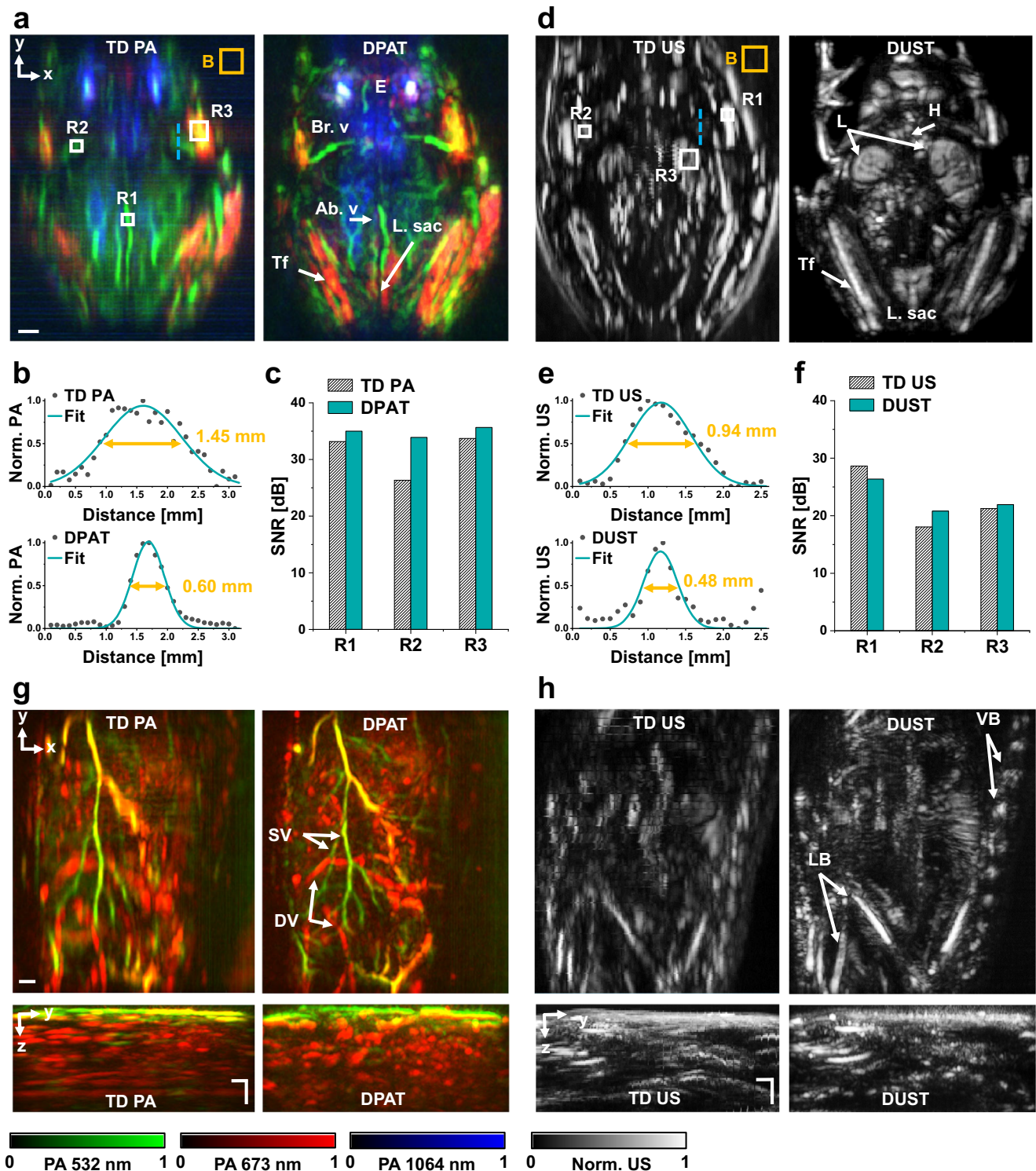


Fig. 3 | 3D-DAT of glassfrog and mouse in vivo. a Multispectral images of glassfrog (*Hyalinobatrachium fleischmanni*) by traditional PA imaging and DPAT, acquired at 532 nm (in green), 673 nm (in red), and 1064 nm (in blue). Ab. V, abdominal vein; Br. V, brachial vessels; E, eyes; L.sac, lymphatic sac (pelvic and ventral); Tf, Tibio-fibula. The absorption distribution at 673 nm is responsible for the cyan-green coloration in the lymph and lungs of the glassfrogs. **b** FWHM of the blood vessel marked with the dashed blue line in (a) by TD PA (top) and DPAT (bottom). **c** SNR of three regions of interest marked as 'R1', 'R2', and 'R3' in (a), using the same background region marked as 'B'. **d** Images of the glassfrog by traditional US imaging and DUST. H, heart; L, lungs. **e** FWHM of the bone marked with the

dashed blue line in (d) by TD US imaging (top) and DUST (bottom). **f** SNR of three regions of interest marked as 'R1', 'R2', and 'R3' in (d), using the same background region marked as 'B'. **g** Multispectral imaging of a mouse abdominal region by traditional PA imaging and DPAT, projected along the lateral/elevational view (top) and the elevational/axial view (bottom). DV, deep vessels; SV, superficial vessels. Compared with the traditional PA imaging, DPAT shows a comparable imaging depth and improved elevational resolution. **h** Corresponding images of the mouse by traditional US imaging and DUST, showing comparable imaging depth but improved elevational resolution by DUST. LB, leg bone; VB, vertebrae. Scale bars, 2 mm.

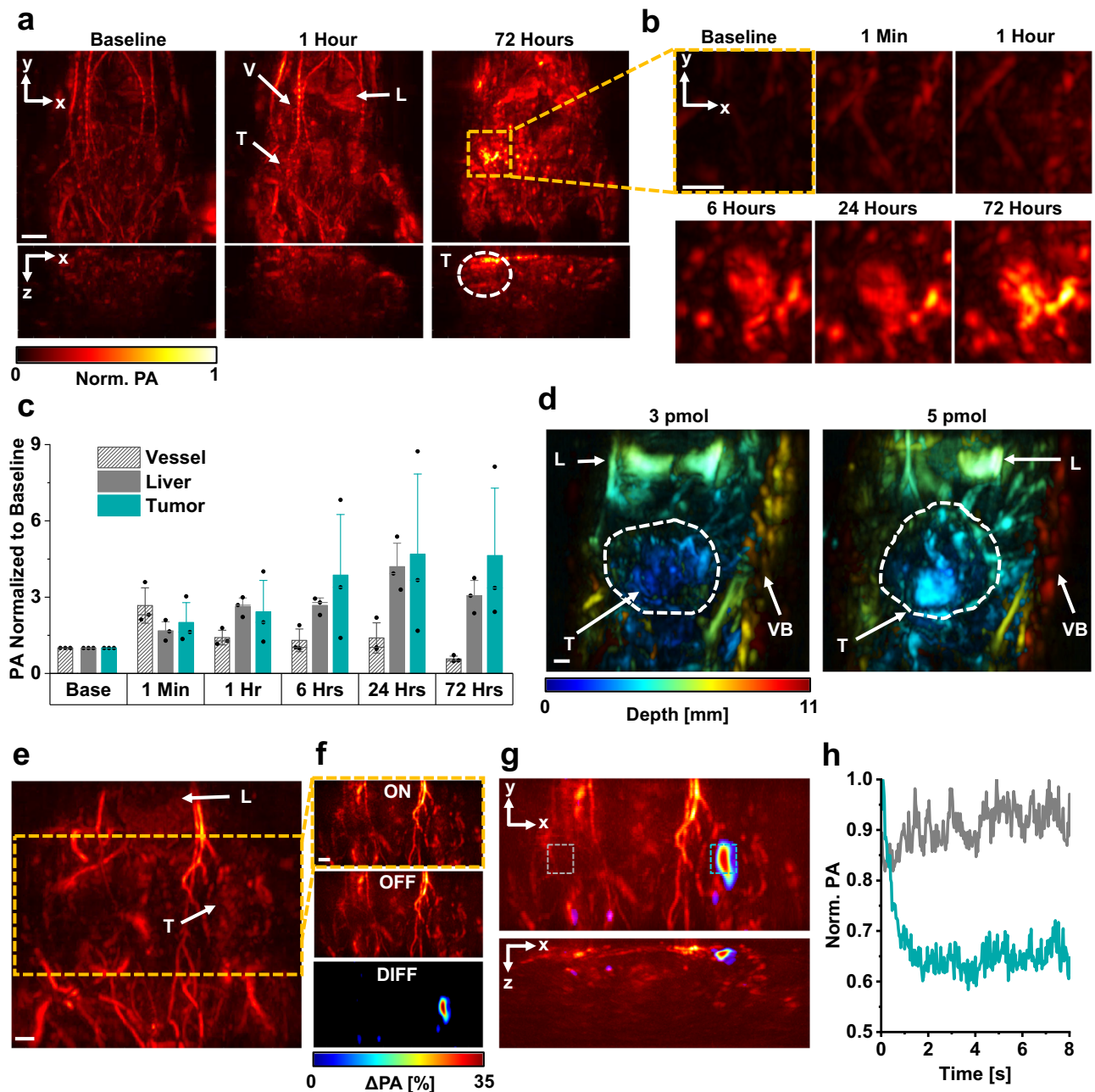


Fig. 4 | In vivo functional and molecular 3D-DAT of murine tumor models.

a DPAT images of the tumor-bearing mouse at baseline, 1 h, and 72 h after cGNS injection. The images were acquired at 700 nm. V, vessel; L, liver; T, tumor. **b** Close-up DPAT images of the tumor region over 72 h, showing gradual accumulation of cGNS inside the tumor. **c** The averaged PA signals in the vessels, liver, and tumor at different time points following cGNS injection ($n = 3$ biological replicates). Error bars show standard deviation. **d** Depth-encoded DPAT images of the tumor, 48 h after injections of cGNS at concentrations of 3 pmol and 5 pmol. VB, vertebrae.

e DPAT image of a mouse at 750 nm bearing a photoswitchable BphP1-expressing tumor (indicated by the dashed box). **f** DPAT images of the BphP1-expressing tumor at the ON-state and OFF-state. The resultant differential image highlights the tumor only while the background signals from blood are suppressed. **g** Coronal and transverse DPAT image of the non-switching blood vessels overlaid with differential image of the photoswitching tumor. **h** PA signal intensity of the tumor region (blue box) and non-tumor region (white box) averaged over 10 photo-switching cycles. Scale bars, 5 mm for (a) and 2 mm for (b)–(f).

(cGNS) integrate the tunable optical properties of GNS with the loading ability of hollow nanoparticles⁴² and have a molar extinction coefficient at 700 nm that is 3 and 10 times higher than oxy- and deoxy-hemoglobin, respectively (Supplementary Fig. 22a, b). As proof of concept, we applied 3D-DAT as a molecular imaging platform for longitudinal monitoring of cGNS biodistribution in a murine 4T1 breast cancer model (Supplementary Fig. 22c). 3D-DAT tracked the whole-body biodistribution of cGNS in tumor-bearing mice ($n = 3$) over 72 h (Fig. 4a, b, and Supplementary Fig. 23). To validate the 3D-DAT result,

we loaded the cGNSs with HITC fluorescent dye and performed fluorescence imaging 48 h after cGNS injection (Supplementary Fig. 22d). From the DPAT results, we found that immediately following the retro-orbital injection of cGNS, there was an average increase of $167 \pm 65\%$ in PA signal intensity in the major blood vessels, with an estimated blood cGNS concentration of ~ 2.2 nM (Fig. 4c). The PA signals in the vessels peaked at 1-min post-injection (Supplementary Movie 8) and returned to the baseline 6 h post-injection. Based on the SNR in the blood vessels, we estimated that the noise-equivalent

detection sensitivity of DPAT for cGNS in blood is 0.65 nM. cGNS accumulation in the liver peaked after 24 h, resulting in an average PA intensity increase of $320 \pm 87\%$. cGNS accumulation in the tumor also peaked after 24 h, with an average PA intensity increase of $369 \pm 297\%$ (Fig. 4b, c).

DPAT was also used to monitor the cGNS accumulation in the liver and tumor 48 h post-injection of a 3- or 5-picomole injection dose (Fig. 4d and Supplementary Fig. 24a). Corresponding fluorescence images were acquired to validate the accumulation of cGNS (Supplementary Fig. 24b). We found that the PA signal in the tumor increased approximately proportionally to the injection dose (Supplementary Fig. 24c), consistent with the cGNS kinetics study (Fig. 4a, b).

Solid tumors are known to exist in hypoxic conditions due to poorly constructed vessels and rapid cell division⁴³. Tumor oxygenation can be a predictor of stage, severity, and likelihood of metastasis in many cancers^{44–46}. Thus, the ability to noninvasively quantify tumor oxygenation in vivo provides a crucial parameter for cancer evaluation. Using multispectral DPAT, in addition to monitoring the cGNS accumulation, we also estimated tumor oxygenation in vivo ($n = 3$) (Supplementary Fig. 25a). As expected, the average sO_2 in the tumor region was $39 \pm 2\%$, compared to the average sO_2 of $58 \pm 9\%$ in the surrounding vessels (Supplementary Fig. 25b and Supplementary Note 7), showing significantly reduced oxygenation in the tumors ($p = 0.0484$). Using the functional and molecular imaging of DPAT, we were able to investigate the tumor hypoxia and the cGNS accumulation inside the tumor, both of which partially originated from the poorly developed tumor vasculature system.

Imaging genetically encoded reporters has enabled major applications in life sciences^{47–49}. Non-fluorescent photoswitching bacterial phytochromes from the bacterium *Rhodospseudomonas palustris*, such as BphP1, have previously been used as genetically encoded reporters in photoacoustic imaging^{50,51}. BphP1 has two conformational states with different optical spectra: Pfr and Pr (Supplementary Fig. 26a), as a result of photoisomerization of biliverdin IX α . By repeatedly photoswitching BphP1-expressing tumor cells between the Pfr and Pr states, we can isolate the weak BphP1 signals from the tumor by taking the differential images, which suppress the strong non-photoswitching background signals from hemoglobin and improve the detection sensitivity of BphP1 (Supplementary Fig. 26b). We first validated the feasibility of photoswitching DPAT (PS-DPAT) in a BphP1-expressing tumor phantom (Supplementary Fig. 26c, Supplementary Movie 9). We observed an average photoswitching ratio of ~ 2 for the in-vitro tumor cells (Supplementary Fig. 26d, e). We then applied PS-DPAT to detect a BphP1-expressing breast tumor in vivo (Fig. 4e, f, Supplementary Movie 10). Using multiple photoswitching cycles in the tumor region, we measured an averaged tumor-to-background ratio of 3.55 from the differential image (Fig. 4g) and an average photoswitching ratio of ~ 1.54 in vivo (Fig. 4h). The expression of BphP1 in the tumor was validated via epifluorescence imaging, which, however, has much lower spatial resolution (Supplementary Fig. 27).

3D-DAT of per- and polyfluoroalkyl substances exposure on embryo development

Following the extensive testing and validation of 3D-DAT for functional and molecular imaging, we demonstrated the technique for a feasibility study of the effects of per- and polyfluoroalkyl substances (PFAS) exposure on mouse embryo development. PFAS, also known as ‘forever chemicals’, refers to a class of fluorinated compounds that are abundant in industrial and consumer products⁵². Due to its ubiquity, bioaccumulation, and adverse health effects, PFAS pollution is a significant public health crisis. Pregnant women and their developing fetuses are known to be particularly susceptible to PFAS effects that can lead to increased risk of miscarriage⁵³, low birth weight⁵⁴, and neurobehavioral changes in the offspring⁵⁵. Although the underlying mechanisms of PFAS exposure are not well

understood, the potential role of lipid metabolism⁵⁶ and mitochondrial function^{57,58} has been identified, which may result in altered oxygen metabolism in the placenta and embryo. Using 3D-DAT, we were able to longitudinally examine the oxygenation levels during the development of the embryo throughout pregnancy and investigate how perinatal PFAS exposure via drinking water may affect the oxygenation levels.

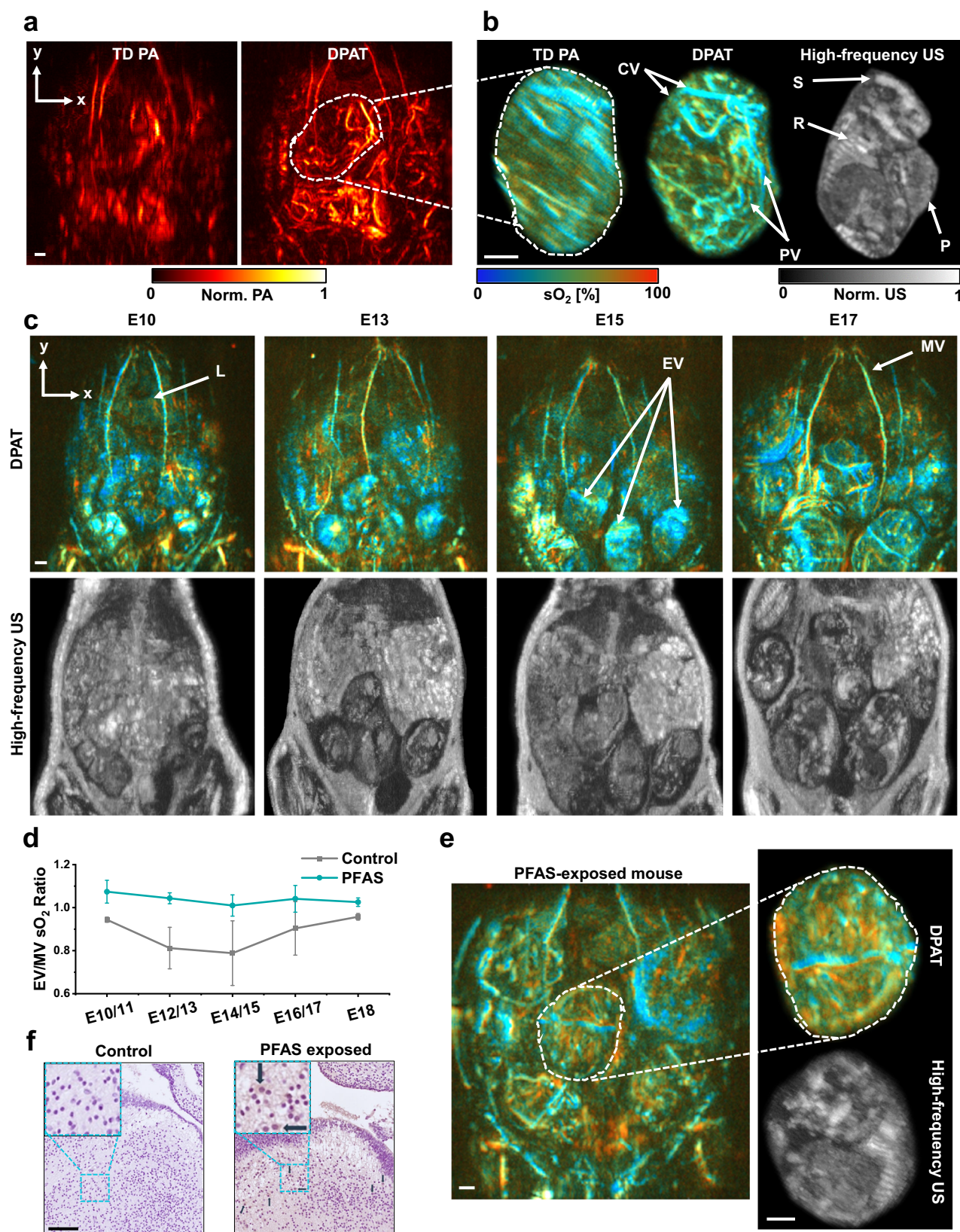
With enhanced elevational resolution, DPAT can better resolve small vascular structures compared to traditional PA imaging (Fig. 5a, b) and provides a better tool for longitudinal functional studies. Pregnant mice were imaged from E8.5 to E18.5, and the embryonic sO_2 was quantified by DPAT (Fig. 5b, c)⁵⁹. DUST images of the embryos were also acquired (Supplementary Fig. 28). Following 3D-DAT, mice were imaged using a high-frequency US imaging system for validating the embryo development (Fig. 5c)⁶⁰. We quantified the ratio of the sO_2 levels in the embryonic vessels (EV) to the maternal vessels (MV) (EV/MV ratio) over gestational days E10.5–E18.5 (Fig. 5d, Supplementary Fig. 29, and Supplementary Fig. 30). Consistent with our previous study⁶¹, we found that the embryos of the control group had an average of 21% lower sO_2 levels from E12–E15 compared to the maternal vessels. We believe that the hypoxic conditions facilitated normal embryonic development by promoting angiogenesis and reducing oxidative stress⁶¹. However, we observed a significantly higher EV/MV ratio for all gestational days in the PFAS group compared with the control group ($p < 0.05$) (Fig. 5d, e and Supplementary Note 7). We hypothesized that the higher oxygenation level in the PFAS group may have negative effects on embryonic growth and development, specifically, the embryo brain development which has high plasticity and is sensitive to oxidative stress⁶².

Following 3D-DAT at E18.5, all mice were sacrificed for further histological analysis. Our data analysis revealed no significant difference in embryo weight, placental weight, or embryo/placenta weight ratio between the control and PFAS group ($p = 0.29, 0.31, 0.64$). No overt pathological differences were appreciated in sagittal sections of embryo brains at E18.5 between the two groups. However, 8-Hydroxy-2'-deoxyguanosine (8OHdG), a validated marker for oxidative stress⁶³, was positive in the embryo brains of the PFAS group (8/18 positive) (Fig. 5f). These histology data corroborated the functional changes in the embryonic oxygenation acquired by DPAT, yet there were no discernible structural changes in the organs. The functional changes observed by DPAT provide an important insight for the mechanisms of developmental and neurobehavioral alterations in rodent offspring exposed to this PFAS mixture discovered in our previous study⁵⁵.

Discussion

We have developed an advanced photoacoustic and ultrasound imaging system, 3D-DAT, which uses single-slit acoustic diffraction to achieve near-isotropic spatial resolutions with an off-the-shelf linear transducer array. Powered by a highly efficient FFL image reconstruction method, 3D-DAT has achieved fast anatomical, functional, and molecular imaging in various proof-of-concept animal models, including transparent glassfrogs, murine tumor models, and pregnant mice. One major advantage of 3D-DAT over existing 3D PA and US imaging systems is the use of the widely available linear ultrasound transducer arrays that ensure high accessibility by the broad research community. 3D-DAT has improved its elevational spatial resolution by 2- to 3-fold over the traditional PA/US imaging with the same linear transducer array, without compromising the field of view, imaging speed, imaging depth, or detection sensitivity.

Compared to 3D PA/US imaging systems using expensive matrix-array transducers, 3D-DAT is much more cost-effective and can be adapted by broad biomedical research fields. In addition to high accessibility, 3D-DAT also solved a longstanding technical dilemma of the matrix-array transducer: the tradeoff of the element size, detection



sensitivity, and densely sampled field of view¹². Often, a matrix-array needs to reduce the element size (e.g., one acoustic wavelength) to enlarge the densely sampled field of view, which leads to reduced detection sensitivity. For example, for a customized 5-MHz matrix array with an element size of 300 μm , its detection sensitivity is at least 20-fold lower than the linear-array transducer used in 3D-DAT. By

contrast, 3D-DAT can achieve a similar spatial resolution and field of view as the matrix-array, but with much improved detection sensitivity and drastically reduced cost.

Compared to traditional linear-array-based PA/US imaging, 3D-DAT has to overcome a few technical tradeoffs. Firstly, the addition of single-slit diffraction, while resulting in improved 3D imaging,

Fig. 5 | Longitudinal 3D-DAT of embryo development when exposed to PFAS during pregnancy. **a** TD PA and corresponding DPAT image, acquired at 700 nm, of a control pregnant mouse at E18.5. **b** A single embryo (indicated by the dashed white line in **(a)**) imaged by traditional PA imaging, DPAT, and high-frequency US imaging. Placental vessels (PV) and cranial vessels (CV) are presented in the DPAT image. The skull (S), ribs (R), and placenta (P) are confirmed in the high-frequency US image. **c** Longitudinal DPAT images of blood oxygenation and high-frequency US images of a control mouse during pregnancy. L, liver; EV, embryo vessel; MV,

maternal vessel. **d** EV/MV blood oxygenation ratio during pregnancy for the control and PFAS-exposed mice ($n = 3$ mice for each group). Error bars show standard deviation. **e** DPAT image of PFAS-exposed mouse at E16 with enlarged region of a single embryo with corresponding high-frequency US image shown on the right. **f** 8OHdG IHC staining in embryo brain sections of the control mice and the PFAS-exposed mice, showing a higher concentration of 8OHdG (brown color) in PFAS-exposed sections (8/18 positive). Arrows indicate positively marked cells. Scale bars, 2 mm for **(a)–(e)**, 100 μm for **(f)**.

degrades the 2D image quality at each single scanning position (i.e., without scanning of the array along the elevational axis). This tradeoff highlights the importance of implementing a 3D-DAT system with a precisely controllable slit. When the slit is wide open, we can still perform single-position 2D imaging. Secondly, 3D-DAT reduces the amount of on-axis acoustic energy that can transmit through the slit towards the transducer. However, due to the enlarged detection angle with the slit present, this signal loss is largely compensated for by integrating over the elevational scanning aperture, resulting in comparable SNR and CNR between 3D-DAT and traditional imaging. Thirdly, to achieve improved image quality, a more computationally expensive reconstruction method is necessary with 3D-DAT. With the efficient FFL reconstruction, 3D-DAT can complete a 3D reconstruction in a few seconds.

The spatial resolution of 3D-DAT is jointly determined by the linear-array transducer's frequency and the slit width. A higher frequency transducer and a smaller slit width can be used for further improving resolution in both DPAT and DUST modes. This will be particularly beneficial for preclinical small-animal imaging applications. 3D-DAT can also be applied to other 1D transducer geometries with poor elevational resolutions, such as the ring-array transducer. Moreover, DUST can be further improved with coherent plane-wave compounding or synthetic aperture imaging to increase both lateral resolution and SNR^{64,65}. Power Doppler US imaging may also be applied with 3D-DAT for isotropic 3D imaging of blood perfusion.

Overall, 3D-DAT is a highly promising and accessible imaging method with structural, functional, and molecular imaging capability in deep tissues, opening doors to studying a variety of physiological phenomena and disease states.

Methods

3D-DAT system

The complete 3D-DAT system configuration is shown in Fig. 1a. High-speed multispectral optical illumination was achieved using three separate lasers. A 532 nm laser (CNI), an optical parametric oscillator (OPO) pumped by a separate 532 nm laser (Continuum), and a 1064 nm laser (Quantel) were all coupled coaxially using dichroic mirrors into two multimode fibers after passing through a beam splitter. Each multimode fiber had 4 outputs, resulting in 8 total outputs from the two bundles. Each fiber bundle had a total output energy of ~2 mJ per pulse for OPO wavelengths in the near infrared (NIR) imaging range, ~200 μJ per pulse for 532 nm, and ~2 mJ per pulse for 1064 nm. The total illuminated region had an area of ~8 cm², giving optical fluence at the surface of the animals far below the American National Standards Institute (ANSI) safety limits at all wavelengths. Each laser was triggered with a field programmable gate array (FPGA) (myRIO, National Instruments) to generate a <10 ns laser pulse with 10 ms between pulses from different lasers. The FPGA was programmed and controlled with the LabVIEW 2018 software (National Instruments). The three lasers were pumped at 10 Hz, allowing for multispectral imaging at a B-scan frame rate of 10 Hz. A power meter (Ophir) was used to measure pulse-by-pulse energy for all wavelengths for pre-reconstruction energy normalization. This was achieved by using a beam sampler to reflect a small amount (<5%) of the light onto the power meter for pulse energy monitoring.

Two pieces of 22 × 60 mm borosilicate cover glass (thickness: 150 μm) (VWR) were sandwiched together using ultraviolet (UV) glue. The UV glue was placed in a continuous line around the four edges of the glass to allow for an air gap between the two pieces when glued together. This improved the overall acoustic impedance of the slit to avoid ultrasound being transmitted directly through the glass. Due to the extremely low optical attenuation of both borosilicate glass and UV glue in the visible and NIR-I spectra, as well as the thinness of the slit assembly, the optical attenuation and refraction by the slit were expected to have minimal effect on the diffuse optical excitation of 3D-DAT. The borosilicate cover glasses that form the slit were each attached to a customized slit stage, such that the slit was at the elevational focus of the linear-array transducer (L7-4, Philips). The slit stage was mounted to a separate motorized stage to allow for concurrent scanning with the linear-array transducer. The customized slit stage was a linear motorized stage controlled by a stepper motor. Two ball screws with opposite threads were joined in the middle to allow for inverse linear motion of opposite halves of the stage. This allowed for the opening and closing of the slit to be controlled by the stepper motor (see Supplementary Movie 1). All ultrasound and photoacoustic data acquisition sequences were controlled with a programmable ultrasound scanner (Vantage 256, Verasonics), programmed with MATLAB 2019b (MathWorks, Inc.).

FFL reconstruction implementation

For in vivo studies, an elevational scanning range of 3–4 cm was used, with a step size of 0.1 mm (300–400 discrete steps). A total depth of ~1 cm was reconstructed, starting approximately at the target surface. The aperture width of the L7-4 linear-array transducer is ~38.4 mm. Therefore, with our reconstruction grid size of [400, 400, 150], our reconstructed voxels had sizes of [0.096, 0.100, 0.067] millimeters in the lateral, elevational, and axial axes, respectively. Nyquist sampling criterion was thus met with these voxel dimensions, given the minimum 400 μm resolution of 3D-DAT (Supplementary Fig. 1). FFL reconstruction was written and executed in MATLAB, using a computer with 256 GB of random-access memory (RAM), an AMD Ryzen Threadripper 3970X central processing unit (CPU) (32 cores, 64 threads), and an NVIDIA RTX A6000 graphics processing unit (GPU) with 48 GB of GDDR6 VRAM and 10,752 CUDA cores.

Validation of 3D-DAT by k-Wave simulation

To theoretically characterize 3D-DAT and determine the relationship between the slit width and image quality, we constructed a 3D ultrasound simulation using the k-Wave MATLAB toolbox (Supplementary Fig. 9)⁶⁶. A synthetic crosshair phantom was scanned across the elevational axis with a step size of 100 μm . The transducer and slit remained stationary, with the slit 25 mm from the transducer surface, corresponding to the elevational focal depth of the L7-4 transducer. At each phantom position, a 3D simulation of ultrasound propagation in the medium was performed. In the case of the DPAT simulation, the cross-hair acted as the initial pressure distribution, and only the propagation of the resultant ultrasound waves was simulated. In the case of the DUST simulation, a plane wave was transmitted from the transducer and the phantom acted as an acoustic reflector in the medium. The simulation was performed for slit widths ranging from 0.3 mm to 1.9 mm.

cGNS synthesis

Silver-coated gold nanostars were prepared using the method described by Fales et al., where 1 mL of 10 nM 12 nm-gold sphere solution is added to 100 mL of 25 μ M HAuCl₄⁶⁷. 500 μ L of 6 mM AgNO₃ followed by 500 μ L of 0.1 M ascorbic acid was rapidly added to the mixture. After 10 s, 500 μ L of 0.1 M AgNO₃ was added, followed by 100 μ L of 30% ammonium hydroxide. After 10 min, 10 mL of 55 mg/mL polyvinylpyrrolidone (PVP) solution was added to the particles, which were then centrifuged and resuspended in 100 mL of 20 mg/mL PVP and 50 mM ascorbic acid solution. 1 mL of NaOH was then added to the mixture. 1.5 mL of 5 mM HAuCl₄ was added via a syringe pump for 30 min. Particles were centrifuged and resuspended in 60 mL of 55 mg/mL PVP solution, and the temperature was increased to 65 °C. Next, 10 mL of 10% hydrogen peroxide solution and 500 μ L of hydrochloric acid were added to the nanoparticle solution and were rapidly mixed for 45 min. Insoluble silver chloride was separated from the cGNS solution via centrifugation, and the particles were washed with 100% ethanol to remove surface-bound PVP. Washed cGNS particles were then concentrated and added to a 1 mg/mL solution of 1,1',3,3',3',3'-Hexamethylindotricarbocyanine iodide (HITC) and allowed to mix overnight. The following day, the particle solution was redispersed into 80 mL of 20 mg/mL PVP solution, followed by 1 mL of 0.1 M ascorbic acid and 100 μ L of HCl. 2 mL of 5 mM HAuCl₄ was then added via a syringe pump for 10 min. Finally, the particles were washed in ethanol several times to remove surface-bound PVP and incubated at 45 °C in a 10 mL of 1 mg/mL SH-PEG₅₀₀₀-COOH solution overnight. Pegylated particles were then washed in DI water and stored at 4 °C until further use.

3D-DAT of cGNS

Before the injection of cGNS, a baseline image of the mouse was acquired using 3D-DAT. For DPAT, the excitation wavelength was 700 nm, which is near the peak absorption of cGNS (Supplementary Fig. 22a). Following the baseline image, either -60 or -100 μ L of cGNS particles with a concentration of 10 mg/mL was administered to each mouse via retro-orbital injection. The mice were then imaged with 3D-DAT at 1 min, 1 h, 6 h, 24 h, and 72 h following the injection of cGNS (Fig. 4b, c, and Supplementary Fig. 23). Fluorescence images of the mice were acquired 48 h after injection to confirm the location of the tumor and accumulation of cGNS respectively. The fluorescence images shown in Supplementary Fig. 22d were taken with an IVIS Kinetic system (PerkinElmer).

A custom-built system was used to acquire fluorescence images of mice that received different cGNS dosages (Supplementary Fig. 24b). The system consisted of an inverted Nikon eclipse Ti-U microscope using a TL2x-SAP long working distance objective. A 785 nm excitation source was used, and the collected light was passed through an 800-nm long-pass filter, where a ProEm 512 camera was used as a detector with an accumulation time of 15 s per location.

PS-DPAT of BphP1 in-vitro and in vivo

PS-DPAT was performed using an OPO laser with a pulse repetition rate (PRR) of 30 Hz (Spitlight, Innolas). First, 630 nm light was illuminated on the target for 8 s through the same fiber bundles used in DPAT. This converts all BphP1 molecules in the illuminated region from Pr to Pfr state. The 630 nm light was then turned off and PA imaging with 750 nm excitation started. As the PA light illuminated the target region, the BphP1 was converted back from the Pfr state to the Pr state. After 240 laser pulses (or 8 s), the transducer was scanned by 0.2 mm to the next elevational position. The 16-second PS cycle was then repeated (Supplementary Fig. 26b). To generate 3D reconstructions at different times during each cycle of Pfr \rightarrow Pr switching process, only corresponding PA pulses were used for each scanning position. Therefore, a total of 240 volumes were reconstructed, showing the complete three-dimensional switching cycle of BphP1.

High-frequency ultrasound imaging

High-frequency ultrasound imaging was performed as validation for the PFAS study. We used the Vega robotic imaging system operating at 25 MHz⁶⁸. The system consists of a high-frequency wobbler transducer made of PVDF, allowing for both high-resolution and high-sensitivity imaging (Supplementary Fig. 28). Before imaging, a 5 mm layer of agarose gel was placed on the imaging membrane, with distilled water for acoustic coupling. The gel pad was placed such that the focus of the wobbler transducer was approximately 2 mm below the skin surface of the mouse torso. The mouse was then placed on top of the gel, and an infrared heating lamp was used to keep the mouse warm. A 40 \times 40 mm² field of view was then scanned, with a total scanning time of approximately 1 min.

Longitudinal imaging of mouse pregnancy and PFAS exposure

The exposure protocol in mice was conducted according to our previous work^{55,69}. The chosen mixture contains 10 different PFAS for a total PFAS concentration of ~758.6 ng/L mimicking highly contaminated drinking water. The 2-month-old female BALB/C mice were exposed to a PFAS mixture one week before breeding and during pregnancy until euthanasia at E18.5. The control female mice were given pure water. The visible vaginal plug was observed to confirm mating and define the embryo day 0.5 (E0.5). 8-9 days following the plug confirmation, longitudinal imaging began with both 3D-DAT and high-frequency ultrasound. Mice were imaged once every 2-3 days until delivery. The weights of mice were also measured during each imaging session. During pregnancy, estimations of gestational days were verified by estimating the crown-rump length (CRL) using high-frequency ultrasound images⁷⁰.

Immunohistochemistry

Embryonal (E18.5) brain samples were paraffin-embedded and cut into 5 μ m-thickness sections. Slides were deparaffined in xylene and rehydrated in serially decreasing concentrations of ethanol and distilled water. Heat-induced antigen retrieval was performed in a citrate-based solution (Antigen Unmasking Solution, Vector Laboratories, Inc, Burlingame, CA, cat# H-3300). Following 2 washes with 1X phosphate buffer saline (PBS), permeabilization of the slides with 0.1% Triton-X in PBS was done. The slides were washed with 1X PBS twice and endogenous peroxidases were blocked by 3% hydrogen peroxide for 30 min at room temperature. This was followed by 4 washes of 1X PBS and blocking slides with 10% goat serum and 1% Bovine Serum Albumin (BSA) in PBS for 20 min at room temperature. Slides were washed with 1X PBS once and incubated with primary antibody 8OHdG (Bioss Antibody, bs-1278R) at 1:200 dilution overnight at 4 degrees in a humidified chamber. After 4 washes with 1X PBS, tissues were incubated with HRP-linked secondary antibody at 1:50 dilution (Goat-Anti-Rabbit Antibody, HRP linked, Bioss Antibody BS-0295G-HRP) at room temperature for 1 h. All the antibodies were diluted in the blocking buffer mentioned above. Subsequently, the slides were washed with 1X PBS 4 times, incubated with DAB substrate at 1:10 dilution (ThermoFisher 34002) for 5 min, washed with pure water, and counterstained with hematoxylin for 10 s. The slides were dehydrated through serially increasing concentrations of ethanol and xylene and mounted with the Permount mounting media (Fischer Scientific SP15). The slides were examined, and images were obtained using the Leica Mica microscope (20x magnification for widefield image, \times 63 magnification for close-up image (Fig. 5f)).

Reporting summary

Further information on research design is available in the Nature Portfolio Reporting Summary linked to this article.

Data availability

All data needed to evaluate the conclusions in the study are present in the paper and/or the Supplementary Materials. Several example datasets have also been deposited to the Zenodo repository and are freely available and accessible.

Code availability

The main reconstruction code and oxygen saturation estimation code have been deposited to the Zenodo repository, with example datasets, and are freely available and accessible.

References

- Wang, L. V. & Yao, J. A practical guide to photoacoustic tomography in the life sciences. *Nat. methods* **13**, 627–638 (2016).
- Beard, P. Biomedical photoacoustic imaging. *Interface focus* **1**, 602–631 (2011).
- Xu, M. & Wang, L. V. Photoacoustic imaging in biomedicine. *Rev. Sci. Instrum.* **77**, 041101 (2006).
- Xu, M. & Wang, L. V. Universal back-projection algorithm for photoacoustic computed tomography. *Phys. Rev. E* **71**, 016706 (2005).
- Tzoumas, S., Deliolanis, N. C., Morscher, S. & Ntziachristos, V. Unmixing molecular agents from absorbing tissue in multispectral photoacoustic tomography. *IEEE Trans. Med. imaging* **33**, 48–60 (2013).
- Li, M. et al. Three-dimensional deep-tissue functional and molecular imaging by integrated photoacoustic, ultrasound, and angiographic tomography (PAUSAT). *IEEE Trans. Med. Imaging* **41**, 2704–2714 (2022).
- Lee, H., Choi, W., Kim, C., Park, B. & Kim, J. Review on ultrasound-guided photoacoustic imaging for complementary analyses of biological systems in vivo. *Exp. Biol. Med.* **248**, 762–774 (2023).
- Li, L. et al. Single-impulse panoramic photoacoustic computed tomography of small-animal whole-body dynamics at high spatio-temporal resolution. *Nat. Biomed. Eng.* **1**, 0071 (2017).
- Merčep, E., Herraiz, J. L., Deán-Ben, X. L. & Razansky, D. Transmission–reflection optoacoustic ultrasound (TROPUS) computed tomography of small animals. *Light.: Sci. Appl.* **8**, 18 (2019).
- Yang, J., Choi, S. & Kim, C. Practical review on photoacoustic computed tomography using curved ultrasound array transducer. *Biomed. Eng. Lett.* **12**, 19–35 (2022).
- Deán-Ben, X. L. et al. Deep optoacoustic localization micro-angiography of ischemic stroke in mice. *Nat. Commun.* **14**, 3584 (2023).
- Yao, J. & Wang, L. V. Perspective on fast-evolving photoacoustic tomography. *J. Biomed. Opt.* **26**, 060602 (2021).
- Kratkiewicz, K., Pattyn, A., Alijabbari, N. & Mehrmohammadi, M. Ultrasound and photoacoustic imaging of breast cancer: clinical systems, challenges, and future outlook. *J. Clin. Med.* **11**, 1165 (2022).
- Lin, L. & Wang, L. V. The emerging role of photoacoustic imaging in clinical oncology. *Rev. Clin. Oncol.* **19**, 365–384 (2022).
- Choi, W., Park, E.-Y., Jeon, S. & Kim, C. Clinical photoacoustic imaging platforms. *Biomed. Eng. Lett.* **8**, 139–155 (2018).
- Ren, D., Li, C., Shi, J. & Chen, R. A review of high-frequency ultrasonic transducers for photoacoustic imaging applications. *IEEE Trans. Ultrason. Ferroelectr. Freq. Control* **69**, 1848–1858 (2021).
- Attia, A. B. E. et al. A review of clinical photoacoustic imaging: current and future trends. *Photoacoustics* **16**, 100144 (2019).
- Wang, Y., Zhan, Y., Tiao, M. & Xia, J. Review of methods to improve the performance of linear array-based photoacoustic tomography. *J. Innovative Opt. Health Sci.* **13**, 2030003 (2020).
- Zheng, W. et al. Deep learning enhanced volumetric photoacoustic imaging of vasculature in human. *Adv. Sci.* **10**, 2301277 (2023).
- Hauptmann, A. & Cox, B. Deep learning in photoacoustic tomography: current approaches and future directions. *J. Biomed. Opt.* **25**, 112903–112903 (2020).
- N. Wang, N. & Yao, J. Sound out the deep clarity: super-resolution photoacoustic imaging at depths. *IEEE Trans. Ultrason. Ferroelectr. Freq. Control* **71** (2024).
- Deng, H., Qiao, H., Dai, Q. & Ma, C. Deep learning in photoacoustic imaging: a review. *J. Biomed. Opt.* **26**, 040901–040901 (2021).
- Wang, Y., Wang, D., Hubbell, R. & Xia, J. Second generation slit-based photoacoustic tomography system for vascular imaging in human. *J. Biophotonics* **10**, 799–804 (2017).
- Zheng, W., Huang, C., Zhang, H. & Xia, J. Slit-based photoacoustic tomography with co-planar light illumination and acoustic detection for high-resolution vascular imaging in human using a linear transducer array. *Biomed. Eng. Lett.* **12**, 125–133 (2022).
- Wang, Y. et al. Slit-enabled linear-array photoacoustic tomography with near isotropic spatial resolution in three dimensions. *Opt. Lett.* **41**, 127–130, (2016).
- Wang, N. et al. A multiplexed 32× 32 2d matrix array transducer for flexible sub-aperture volumetric ultrasound imaging. *IEEE Trans. Biomed. Eng.* **71**, 831–840 (2023).
- Zhang, H. et al. Deep-E: a fully-dense neural network for improving the elevation resolution in linear-array-based photoacoustic tomography. *IEEE Trans. Med. imaging* **41**, 1279–1288 (2021).
- Xia, J. et al. Three-dimensional photoacoustic tomography based on the focal-line concept. *J. Biomed. Opt.* **16**, 090505–090505 (2011).
- Perrot, V., Polichetti, M., Varray, F. & Garcia, D. So you think you can DAS? A viewpoint on delay-and-sum beamforming. *Ultrasonics* **111**, 106309 (2021).
- Taboada, C. et al. Multiple origins of green coloration in frogs mediated by a novel biliverdin-binding serpin. *Proc. Natl Acad. Sci.* **117**, 18574–18581 (2020).
- L. Menozzi. *Sample Code and Datasets for Three-Dimensional Diffractive Acoustic Tomography*, <https://doi.org/10.5281/zenodo.14618224>.
- Cobbold, R. *Foundations of Biomedical Ultrasound* (Oxford University Press, 2007).
- Taboada, C. et al. Glassfrogs conceal blood in their liver to maintain transparency. *Science* **378**, 1315–1320 (2022).
- Vu, T. et al. On the importance of low-frequency signals in functional and molecular photoacoustic computed tomography. *IEEE Trans. Med. Imaging* **43**, 771–783 (2023).
- Weber, J., Beard, P. C. & Bohndiek, S. E. Contrast agents for molecular photoacoustic imaging. *Nat. methods* **13**, 639–650 (2016).
- Du, L., Qin, H., Ma, T., Zhang, T. & Xing, D. “In vivo imaging-guided photothermal/photoacoustic synergistic therapy with bioorthogonal metabolic glycoengineering-activated tumor targeting nanoparticles,”. *Acs Nano* **11**, 8930–8943 (2017).
- Liu, X., Duan, Y. & Liu, B. Nanoparticles as contrast agents for photoacoustic brain imaging. *Aggregate* **2**, 4–19 (2021).
- Song, G. et al. MnCO₃@ BSA-ICG nanoparticles as a magnetic resonance/photoacoustic dual-modal contrast agent for functional imaging of acute ischemic stroke. *Biochem. Biophys. Res. Commun.* **614**, 125–131 (2022).
- Xi, L. et al. Molecular photoacoustic tomography of breast cancer using receptor targeted magnetic iron oxide nanoparticles as contrast agents. *Wiley Online Libr.* **7**, 401–409 (2014).
- Liu, Y. et al. A Plasmonic Gold Nanostar Theranostic Probe for In Vivo Tumor Imaging and Photothermal Therapy. *Theranostics* **5**, 946–960 (2015).
- Yuan, H. et al. Gold nanostars: surfactant-free synthesis, 3D modelling, and two-photon photoluminescence imaging. *Nanotechnology* **23**, 075102 (2012).

42. Canning, A. J. & Tuan, V.-D. Caged Gold Nanostars: a novel plasmonic nanoplatform with potential theranostic applications. *Nanoscale* **16**, 8828–8835 (2024).
43. Muz, B., de la Puente, P., Azab, F. & Azab, A. K. The role of hypoxia in cancer progression, angiogenesis, metastasis, and resistance to therapy. *Hypoxia* **3**, 83 (2015).
44. Becker, A. et al. Severe anemia is associated with poor tumor oxygenation in head and neck squamous cell carcinomas. *Int. J. Radiat. Oncol. Biol. Phys.* **46**, 459–466 (2000).
45. Brizel, D. M. et al. Tumor oxygenation predicts for the likelihood of distant metastases in human soft tissue sarcoma. *Cancer Res.* **56**, 941–943 (1996).
46. Brizel, D. M., Dodge, R. K., Clough, R. W. & Dewhirst, M. W. Oxygenation of head and neck cancer: changes during radiotherapy and impact on treatment outcome. *Radiother. Oncol.* **53**, 113–117 (1999).
47. Gross, S. and D. Piwnica-Worms, “Spying on cancer: molecular imaging in vivo with genetically encoded reporters,.” *Cancer Cell* **7**, 5–15 (2005).
48. Mank, M. et al. A genetically encoded calcium indicator for chronic in vivo two-photon imaging. *Nat. Methods* **5**, 805–811 (2008).
49. Sabatini, B. L. & Tian, L. Imaging neurotransmitter and neuromodulator dynamics in vivo with genetically encoded indicators. *Neuron* **108**, 17–32 (2020).
50. Kasatkina, L. A. et al. Optogenetic manipulation and photoacoustic imaging using a near-infrared transgenic mouse model. *Nat. Commun.* **13**, 2813 (2022).
51. Yao, J. et al. Multiscale photoacoustic tomography using reversibly switchable bacterial phytochrome as a near-infrared photochromic probe. *Nat. Methods* **13**, 67–73 (2016).
52. Kurwadkar, S. et al. Per- and polyfluoroalkyl substances in water and wastewater: A critical review of their global occurrence and distribution. *Sci. Total Environ.* **809**, 151003 (2022).
53. Chambers, W. S., Hopkins, J. G. & Richards, S. M. A review of per- and polyfluorinated alkyl substance impairment of reproduction. *Front. Toxicol.* **3**, 732436 (2021).
54. Zhang, Y. et al. Association of early pregnancy perfluoroalkyl and polyfluoroalkyl substance exposure with birth outcomes. *JAMA Netw. Open* **6**, e2314934–e2314934 (2023).
55. Marchese, M. J. et al. Prenatal and perinatal exposure to Per- and polyfluoroalkyl substances (PFAS)-contaminated drinking water impacts offspring neurobehavior and development. *Sci. Total Environ.* **917**, 170459 (2024).
56. Yao, W. et al. The developmental toxicity of perfluorohexane sulfonate at human relevant dose during pregnancy via disruption in placental lipid homeostasis. *Environ. Int.* **177**, 108014 (2023).
57. Dong, Z. et al. Perfluorooctane sulfonate induces mitochondrial calcium overload and early hepatic insulin resistance via autophagy/detyrosinated alpha-tubulin-regulated IP3R2-VDAC1-MICU1 interaction. *Sci. Total Environ.* **825**, 153933 (2022).
58. Wei, K.-N. et al. Perfluorooctane sulfonate affects mouse oocyte maturation in vitro by promoting oxidative stress and apoptosis induced by mitochondrial dysfunction. *Ecotoxicol. Environ. Saf.* **225**, 112807 (2021).
59. Li, M., Tang, Y. & Yao, J. Photoacoustic tomography of blood oxygenation: a mini review. *Photoacoustics* **10**, 65–73 (2018).
60. Menozzi, L. et al. Three-dimensional non-invasive brain imaging of ischemic stroke by integrated photoacoustic, ultrasound and angiographic tomography (PAUSAT). *Photoacoustics* **29**, 100444 (2022).
61. Zhu, X. et al. Longitudinal intravital imaging of mouse placenta. *Sci. Adv.* **10**, eadk1278 (2024).
62. Wang, Y. et al. Fetal exposure to dichloroacetic acid and impaired cognitive function in the adulthood. *Brain Behav.* **10**, e01801 (2020).
63. Valavanidis, A., Vlachogianni, T. & Fiotakis, C. 8-hydroxy-2'-deoxyguanosine (8-OHdG): a critical biomarker of oxidative stress and carcinogenesis. *J. Environ. Sci. Health Part C* **27**, 120–139 (2009).
64. Montaldo, G., Tanter, M., Bercoff, J., Benech, N. & Fink, M. Coherent plane-wave compounding for very high frame rate ultrasonography and transient elastography. *IEEE Trans. Ultrason. Ferroelectr. Freq. Control* **56**, 489–506 (2009).
65. Jensen, J. A., Nikolov, S. I., Gammelmark, K. L. & Pedersen, M. H. Synthetic aperture ultrasound imaging. *Ultrasonics* **44**, e5–e15 (2006).
66. Treeby, B. E. & Cox, B. T. k-Wave: MATLAB toolbox for the simulation and reconstruction of photoacoustic wave fields. *J. Biomed. Opt.* **15**, 021314–021314 (2010).
67. Fales, A. M., Yuan, H. & Vo-Dinh, T. Development of hybrid silver-coated gold nanostars for nonaggregated surface-enhanced Raman scattering. *J. Phys. Chem. C: Nanomater Interfaces* **118**, 3708–3715 (2014). Feb 20.
68. Czernuszewicz, T. J. et al. A new preclinical ultrasound platform for widefield 3D imaging of rodents. *Rev. Sci. Instrum.* **89**, 075107 (2018).
69. Crute, C. E. et al. Evaluating maternal exposure to an environmental per and polyfluoroalkyl substances (PFAS) mixture during pregnancy: adverse maternal and fetoplacental effects in a New Zealand White (NZW) rabbit model. *Sci. Total Environ.* **838**, 156499 (2022).
70. Mu, J., Slevin, J. C., Qu, D., McCormick, S. & Adamson, S. L. In vivo quantification of embryonic and placental growth during gestation in mice using micro-ultrasound. *Reprod. Biol. Endocrinol.* **6**, 1–13 (2008).

Acknowledgements

The authors would like to thank Professor Vladislav Verkhusha for his technical support on the photoswitching cells. This work was partially sponsored by the United States National Institutes of Health (NIH) grants RF1 NS115581, R01 NS111039, R01 EB028143, R01 DK139109, R01 DK052985, R01 MH135932, HHSN273201400015C; The United States National Science Foundation (NSF) CAREER award 2144788; Duke University Pratt Beyond the Horizon Grant; Eli Lilly Research Award Program; Chan Zuckerberg Initiative Grant (2020-226178 and 2024-349531); Duke University DST Spark Seed Grant; Duke Coulter Translational Grant; North Carolina Biotechnology Center Translational Research Grant (2024-TRG-0041), all awarded to J.Y. Additionally, this work was partially supported by the United States NSF GRFP award DGE 2139754, awarded to L.M.

Author contributions

L.M., T.V., and J.Y. conceived the idea. L.M. and T.V. designed the imaging system and performed all imaging studies. L.M. designed the FFL reconstruction algorithm and performed numerical simulations. L.M., T.V., C.T. and J.D. performed glassfrog study. A.J.C., J.C., G.M.P. and T.V.D. developed and designed cGNS. A.J.C., J.C., T.C., C.M., and Y.X. developed tumor models and performed fluorescence imaging. L.M., T.V., A.J.C., V.T.N., S.W.C., and P.T. processed visualizations. J.X. contributed to data analysis. L.M., T.V., H.R., M.E.A.A., and L.F. conducted pregnancy study. H.R. and L.F. performed pregnancy histology. L.M. and J.Y. wrote the manuscript with input from all authors. J. Y. supervised the whole study.

Competing interests

T.V., L.M., and J.Y. have financial interests with Lumius Imaging, Inc., which did not support this work. Other authors declare no competing interests.

Additional information

Supplementary information The online version contains supplementary material available at <https://doi.org/10.1038/s41467-025-56435-3>.

Correspondence and requests for materials should be addressed to Tuan Vo-Dinh, Liping Feng or Junjie Yao.

Peer review information *Nature Communications* thanks Sandeep Kumar Kalva and the other, anonymous, reviewer(s) for their contribution to the peer review of this work. A peer review file is available.

Reprints and permissions information is available at <http://www.nature.com/reprints>

Publisher's note Springer Nature remains neutral with regard to jurisdictional claims in published maps and institutional affiliations.

Open Access This article is licensed under a Creative Commons Attribution-NonCommercial-NoDerivatives 4.0 International License, which permits any non-commercial use, sharing, distribution and reproduction in any medium or format, as long as you give appropriate credit to the original author(s) and the source, provide a link to the Creative Commons licence, and indicate if you modified the licensed material. You do not have permission under this licence to share adapted material derived from this article or parts of it. The images or other third party material in this article are included in the article's Creative Commons licence, unless indicated otherwise in a credit line to the material. If material is not included in the article's Creative Commons licence and your intended use is not permitted by statutory regulation or exceeds the permitted use, you will need to obtain permission directly from the copyright holder. To view a copy of this licence, visit <http://creativecommons.org/licenses/by-nc-nd/4.0/>.

© The Author(s) 2025